

Atoms with one and two active electrons in strong laser fields

I. A. IVANOV AND A. S. KHEIFETS

4.1 Introduction

Recent years have witnessed a remarkable progress in high-power short laser pulse generation. Modern conventional and free-electron laser (FEL) systems provide peak light intensities of the order of 10^{20} W cm⁻² or above in pulses in femtosecond and sub-femtosecond regimes. The field strength at these intensities is a hundred times the Coulomb field, binding the ground-state electron in the hydrogen atom. These extreme photon densities allow highly non-linear multiphoton processes, such as above-threshold ionization (ATI), high harmonic generation (HHG), laser-induced tunneling, multiple ionization and others, where up to a few hundred photons can be absorbed from the laser field. In parallel with these experimental developments, massive efforts have been undertaken to unveil the precise physical mechanisms behind multiphoton ionization (MPI) and other strong-field ionization phenomena. It was shown convincingly that multiple ionization of atoms by an ultrashort intense laser pulse is a process in which the highly non-linear interaction between the electrons and the external field is closely interrelated with the few-body correlated dynamics [1]. A theoretical description of such processes requires development of new theoretical methods to simultaneously account for the field nonlinearity and the long-ranged Coulomb interaction between the particles.

In this chapter, we review our recent theoretical work in which we develop explicitly time-dependent, non-perturbative methods to treat MPI processes in many-electron atoms. These methods are based on numerical solution of the time-dependent Schrödinger equation (TDSE) for a target atom or molecule in the presence of an electromagnetic and/or static electric field. Projecting this solution onto final field-free target states gives us probabilities and cross sections for various ionization channels.

The chapter is organized as follows. In Section 4.2 we present the key ingredients of our formalism and its numerical implementation. The next sections cover various applications:

- Section 4.3: Two-photon double ionization of helium
- Section 4.4: DC-assisted double photoionization of He and H⁻
- Section 4.6: ATI and HHG in quasi one- and two-electron atoms
- Section 4.5: Strong-field ionization of lithium
- Section 4.7: Time delay in atomic photoemission

4.2 Theoretical model

We seek a solution of the time-dependent Schrödinger equation for an atom in the presence of an external electromagnetic (EM) field:

$$i \frac{\partial \Psi}{\partial t} = (\hat{H}_{\text{atom}} + \hat{H}_{\text{int}}(t)) \Psi, \quad (4.1)$$

where \hat{H}_{atom} is the field-free Hamiltonian and the operator $\hat{H}_{\text{int}}(t)$ describes interaction of the atom and the EM field. The Hamiltonian of the field-free atomic system can be a completely *ab initio* operator as in the cases of the hydrogen and helium atoms or the hydrogen molecule. For many-electron targets, we apply a frozen core approximation and freeze all the atomic electrons except the valence shell which can contain one or two electrons. This reduces the atomic Hamiltonian to an effective one- or two-body operator. The interaction Hamiltonian $\hat{H}_{\text{int}}(t)$ can be written in various gauges, which are all formally equivalent. We will be using the length and velocity gauges that take the following forms for an n -electron target:

$$\hat{H}_{\text{int}}(t) = \begin{cases} \mathbf{E}(t) \cdot \sum_{i=1}^n \mathbf{r}_i, & \text{length} \\ A(t) \cdot \sum_{i=1}^n \hat{\mathbf{p}}_i, & \text{velocity.} \end{cases} \quad (4.2)$$

Here the vector potential and the electric field are related via

$$\mathbf{A}(t) = - \int_0^t \mathbf{E}(\tau) d\tau.$$

The time dependence of the electric field is chosen to be

$$\mathbf{E}(t) = f(t) \mathbf{E}_0 \cos(\omega t + \phi),$$

where ϕ is a carrier envelope phase (CEP), ω is the carrier frequency, and $f(t)$ is an envelope function that is smooth and slowly varying over the interval $(0, T_1)$, thus ensuring that no artificial transient effects are introduced in the calculation. The field is switched off for $t < 0$ and $t > T_1$. In the case of a long pulse $T_1 \gg T = 2\pi/\omega$,

neither a precise form of $f(t)$ nor the value of the CEP are important. For short pulses $T_1 \gtrsim T$, the pulse shape and the CEP both have a considerable effect.

We seek a solution of the TDSE on the basis of one- or two-electron wave functions

$$\Psi(\mathbf{r}, t) = \sum_{j \equiv \{nlm\} \notin \text{core}} a_j(t) R_{nl}(r) Y_{lm}(\theta, \phi) \quad (4.3)$$

$$\Psi(\mathbf{r}_1, \mathbf{r}_2, t) = \sum_{j \equiv \{n_1 n_2 l_1 l_2 JM\} \notin \text{core}} a_j(t) \left[1 + \hat{P}_{12} \right] R_{n_1 l_1}(r_1) R_{n_2 l_2}(r_2) |l_1(1) l_2(2) JM\rangle \quad (4.4)$$

for atomic systems with one and two valence electrons, respectively. In the one-electron case, the angular dependence is carried by the spherical functions $Y_{lm}(\theta, \phi)$, whereas in the two-electron case it is assumed by the bipolar harmonics $|l_1(1) l_2(2) JM\rangle$ [2]. The spatial exchange operator $1 + \hat{P}_{12}$ ensures the proper symmetrization of the wave function (4.4). Convergence of expansions (4.3–4.4) with respect to the angular momenta depends on the nature of the problem at hand and the ionization regime that we consider. It is known that this converges is generally faster if the velocity gauge is employed for the interaction Hamiltonian [3].

The radial orbitals entering Eqs. (4.3–4.4) are represented by a square-integrable L^2 basis. This basis can be formed in two different ways. One way is to use a set of B-splines of a certain order ($k = 7$) with the knots located on a sequence of points lying in $[0, R_{\max}]$. Another way is to build a set of positive and negative energy pseudostates of size N , which diagonalizes the target Hamiltonian. A basis-based calculation converges when N is sufficiently large.

As an alternative computational strategy, we may discretize the Hamiltonian and the wave functions on a radial grid of sufficient density and extent R_{\max} and seek a direct solution in the form:

$$\Psi(\mathbf{r}, t) = \sum_{lm} R_{lm}(r, t) Y_{lm}(\theta, \phi) \quad (4.5)$$

$$\Psi(\mathbf{r}_1, \mathbf{r}_2, t) = \sum_{l_1 l_2 JM} R_{l_1 l_2 JM}(r_1, r_2, t) |l_1(1) l_2(2) JM\rangle, \quad (4.6)$$

Both grid-based and basis methods of finding the radial solution of the TDSE give us a coupled system of differential equations. The TDSE is solved directly relative to the functions $R_{lm}(r, t)$ or $R_{l_1 l_2 JM}(r_1, r_2, t)$ if we use a grid-based technique, Eqs. (4.5–4.6), or the coefficients of the basis set expansions are obtained if we employ a basis set method, Eqs. (4.3–4.4). In both cases, we can write this system of differential equations in a vector form:

$$i\dot{\mathbf{a}} = (\mathbf{H}_{\text{atom}} + \mathbf{H}_{\text{int}}) \cdot \mathbf{a}, \quad (4.7)$$

where \mathbf{H}_{atom} and $\mathbf{H}_{\text{int}}(t)$ are matrices of the atomic Hamiltonian and the operator of electromagnetic interaction, respectively. A short time propagator for this system can be obtained by using the leading term of the Magnus expansion [4]

$$\begin{aligned} \mathbf{a}(t + \Delta) &\approx \exp \left[-i \int_t^{t+\Delta} \mathbf{H}(\tau) d\tau \right] \\ &\approx \exp [-i \mathbf{H}(t + \Delta/2) \Delta] \mathbf{a}(t) + o(\Delta^2). \end{aligned}$$

To compute an exponential of a large matrix efficiently, we employ the so-called Arnoldi–Lanczos method (ALM) [5, 6]. This technique represents the vector $\mathbf{a}(t + \Delta)$ as a sum of vectors $\mathbf{H}(t)\mathbf{a}(t)$, $\mathbf{H}^2(t)\mathbf{a}(t)$, \dots , $\mathbf{H}^m(t)\mathbf{a}(t)$, forming the Krylov subspace. The procedure is unconditionally stable and explicit, which allows us to treat large-scale computational problems efficiently. As an alternative approach, we can approximate the exponential operator in the Magnus expansion by $[1 - i\mathbf{H}(t + \Delta/2)\Delta/2][1 + i\mathbf{H}(t + \Delta/2)\Delta/2]^{-1}$ with the same accuracy to within the terms of the order of Δ^2 . To evaluate the matrix inverse, we employ the so-called matrix iteration method (MIM) [7], which makes use of the fact that the operator in the denominator can be split as: $1 + i\mathbf{H}(t + \Delta/2)\Delta/2 = \mathbf{A} + \mathbf{B}$, where $\mathbf{A} = 1 + i\mathbf{H}_{\text{atom}}\Delta/2$ and $\mathbf{B} = i\mathbf{H}_{\text{int}}(t + \Delta/2)\Delta/2$, and expanded into the Neumann series:

$$(\mathbf{A} + \mathbf{B})^{-1} = \mathbf{A}^{-1} - \mathbf{A}^{-1}\mathbf{B}\mathbf{A}^{-1} + \mathbf{A}^{-1}\mathbf{B}\mathbf{A}^{-1}\mathbf{B}\mathbf{A}^{-1} \dots \quad (4.8)$$

Terms of this expansion are easily computed to any order. On every step, one has to compute only an inverse of the operator \mathbf{A} , which can be done fast and efficiently.

The bound atomic or molecular state, which gives the initial condition for this system of differential equations, is obtained by using a relaxation procedure in imaginary time for the grid-based calculation, or is prepared by direct diagonalization of the Hamiltonian in the case of a basis set calculation.

Knowing the solution of the TDSE after the end of the pulse $t = T_1$, we obtain various differential ionization probabilities by projecting this solution on a set of states describing the given ionization channel. This procedure is fairly straightforward in the case of an effective one-electron system where the continuum wave functions can be easily calculated. It is much more difficult in the case of double ionization of the helium or hydrogen molecule, where continuous spectra corresponding to single and double ionization may overlap. This issue is addressed in the corresponding sections below.

4.3 Two-photon double ionization of helium

The direct (non-sequential) two-photon double-electron ionization (TPDI) of helium is the simplest and the most fundamental strong-field ionization process

with several active electrons, which requires a non-perturbative treatment of the external field as well as a proper account of correlation in the two-electron continuum. Because of the canonical importance of this process, a large number of theoretical methods have been developed and applied to TPDI of He in recent years. These studies allowed us to achieve considerable progress in understanding the qualitative features of the TDPI phenomenon. However, as far as the quantitative description of TDPI is concerned, the available theoretical results paint a somewhat controversial picture. Even though the total TPDI cross section has been measured in He by using the HHG [8, 9] or FEL [10] sources of radiation, the experimental results still remain debatable [11].

In our approach to the TPDI process in He [12], we seek a solution of the two-electron TDSE in the form of the expansion (4.4) in which functions $R_{l_1 l_2 J M}(r_1, r_2, t)$ are expanded on a basis built from the one-electron radial orbitals $\phi_{nl}^N(r)$. The latter are obtained by diagonalizing the He^+ Hamiltonian in a Laguerre basis of size N [13]:

$$\langle \phi_{nl}^N | \hat{H}_{\text{He}^+} | \phi_{n'l'}^N \rangle = E_{nl} \delta_{nn'} \delta_{ll'}. \quad (4.9)$$

In the present work, we consider an electric field of the order of 0.1 a.u. corresponding to 3.5×10^{14} W/cm² intensity. For this not very high field intensity, we can retain in the expansion (4.4) only the terms with total angular momentum $J = 0-2$. To represent each total angular momentum block, we proceed as follows. For all S , P , D total angular momentum states we let l_1, l_2 vary within the limits 0–3. The total number of pseudostates participating in building the basis states was 20 for each l . To represent $J = 0, 1, 2$ singlet states in expansion (4.4), we used all possible combinations of these pseudostates. Such a choice gave us 840 basis states of S -symmetry, 1200 basis states of P -symmetry and 1430 states of D -symmetry, resulting in a total dimension of the basis equal to 3470. Issues related to the convergence of the calculation with respect to the variations of the composition of the basis set are described in detail in [14].

Initial conditions for the solution of TDSE are determined by solving an eigenvalue problem using a subset of basis functions of the S -symmetry only. This produces the ground-state energy of -2.90330 a.u. We integrate TDSE up to a time T_1 when the external field is switched off. Then we project the solution onto a field-free CCC wave function $\Psi(\mathbf{k}_1, \mathbf{k}_2)$ representing electron scattering on the He^+ ion. Details of the construction of these functions can be found in [15]. This projection gives us a probability distribution function $p(\mathbf{k}_1, \mathbf{k}_2)$ of finding the helium atom in a field-free two-electron continuum state $\mathbf{k}_1, \mathbf{k}_2$ at the time $t = T_1$. From this probability, we can compute various differential and total integrated cross

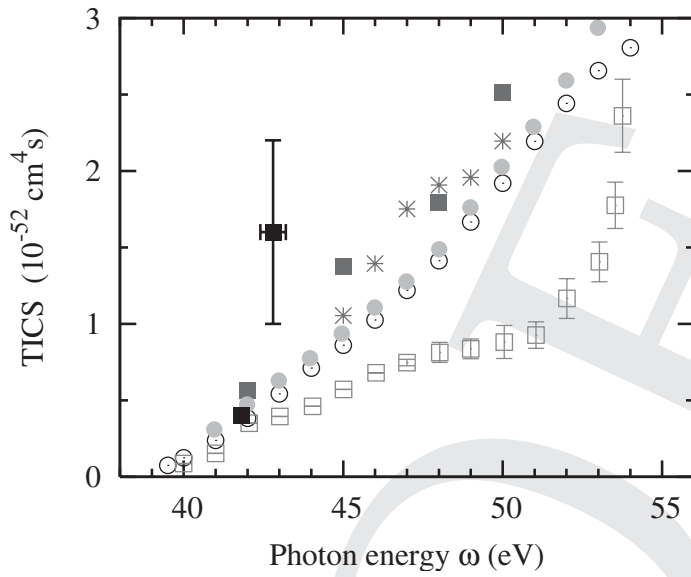


Figure 4.1 Total integrated cross section of TPDI of helium as a function of photon energy. The present TDSE-CCC results (in velocity gauge) are displayed with filled squares. The asterisks display an analogous TDSE calculation with an uncorrelated final state. The literature data are plotted with the following symbols: ECS [16] – open squares, FEDVR-a [17] – open circles, FEDVR-b [18] – filled circles. The experimental data (filled squares) are from [8, 10].

sections (TICS) of TPDI. The latter is computed as

$$\sigma(\omega) = \frac{C}{W} \int p(\mathbf{k}_1, \mathbf{k}_2) d\hat{\mathbf{k}}_1 d\hat{\mathbf{k}}_2 dk_1 dk_2. \quad (4.10)$$

Here $W = \int_0^{T_1} E^4(t) dt$, and $C = 12\pi^2 a_0^4 \tau \omega^2 c^{-2}$ is the TPDI constant expressed in terms of the speed of light in atomic units $c \approx 137$, the Bohr radius $a_0 = 0.529 \times 10^{-8}$ cm and the atomic unit of time $\tau = 2.418 \times 10^{-17}$ s.

The TICS results for TPDI of He are presented in Fig. 4.1, along with the most recent calculations reported in the literature: exterior complex scaling (ECS) [16], finite element discrete variable representation (FEDVR-a) [17] and (FEDVR-b) [18] and the experiment [8, 10]. In the same figure, we also plot an alternative set of our results obtained by projecting the solution of the TDSE on the uncorrelated two-electron final state. This state is represented by the product of the two Coulomb waves. Both sets of our TDSE calculations are fairly close. The issue of the final-state correlation in the TPDI process is discussed in detail in [19].

4.4 DC-assisted double photoionization of He and H^-

Single-photon double ionization (double photoionization – DPI) of helium has been studied extensively over the past decade. Basic mechanisms of this process are now

well understood, both qualitatively and quantitatively, with accurate theoretical predictions being confirmed experimentally under a wide range of kinematical conditions [20, 21]. The emphasis in DPI studies is now shifting towards the multiphoton processes in stronger electromagnetic fields or/and more complex atomic and molecular targets where electron correlation may play a more prominent role. In our work [14], we introduced another factor which would complicate the DPI process: a static electric field. We consider the DPI of helium subjected to an external DC field with the strength ranging from a few hundreds to a few tens of the atomic unit. Since the two-electron escape is a ‘balancing act’ between the inter-electron repulsion and the nucleus drag, the static field may upset this delicate balance or open up new possible two-electron escape routes. This can result in a net decrease or increase of the DPI cross section and changing energy and angular distribution of the photoelectron pair.

The DC-assisted DPI of He is described by the TDSE containing interaction with the external electromagnetic (AC) and static (DC) fields:

$$\hat{H}_{\text{int}}(t) = f(t)(\mathbf{r}_1 + \mathbf{r}_2) \cdot (\mathbf{E}_{\text{AC}} \cos \omega t + \mathbf{E}_{\text{DC}}). \quad (4.11)$$

For simplicity, we consider the case when both the AC and DC fields are parallel and controlled by the same smooth switching function $f(t)$, which turns them on and off during one period of the AC field oscillation $T = 2\pi/\omega$ and keeps them constant on the time interval $(T, 4T)$. The total duration of the atom-field interaction is therefore $T_1 = 6T$. Solution of the TDSE is sought on the pseudostate Laguerre basis [13]. The field-free evolution of the two-electron continuum is described by the CCC wave function $\Psi(\mathbf{k}_1, \mathbf{k}_2)$ representing electron scattering on the He^+ ion [15]. By projecting the solution of the TDSE on this function, we obtain a probability distribution function $p(\mathbf{k}_1, \mathbf{k}_2)$ of finding the helium atom in a field-free state $(\mathbf{k}_1, \mathbf{k}_2)$ at the time $t = T_1$. The DPI cross section is related to the distribution function $p(\mathbf{k}_1, \mathbf{k}_2)$ normalized to the field intensity:

$$\sigma(\mathbf{k}_1, \mathbf{k}_2) = \frac{8\pi\omega}{c} \frac{p(\mathbf{k}_1, \mathbf{k}_2)}{W}, \quad (4.12)$$

where $W = 2 \int_0^{T_1} E_{\text{AC}}^2(t) dt$ and $c \approx 137$ is the speed of light in atomic units. The total integrated cross section (TICS) is given by:

$$\sigma(\omega) = \frac{1}{2} \int \sigma(\mathbf{k}_1, \mathbf{k}_2) d\hat{\mathbf{k}}_1 d\hat{\mathbf{k}}_2 dk_1 dk_2. \quad (4.13)$$

In the present work, we consider modestly strong electric fields: the AC field of the order of 0.1 a.u. corresponding to 3.5×10^{14} W/cm² intensity, and the DC field not exceeding 0.03 a.u. This allows us to retain terms with total angular momentum

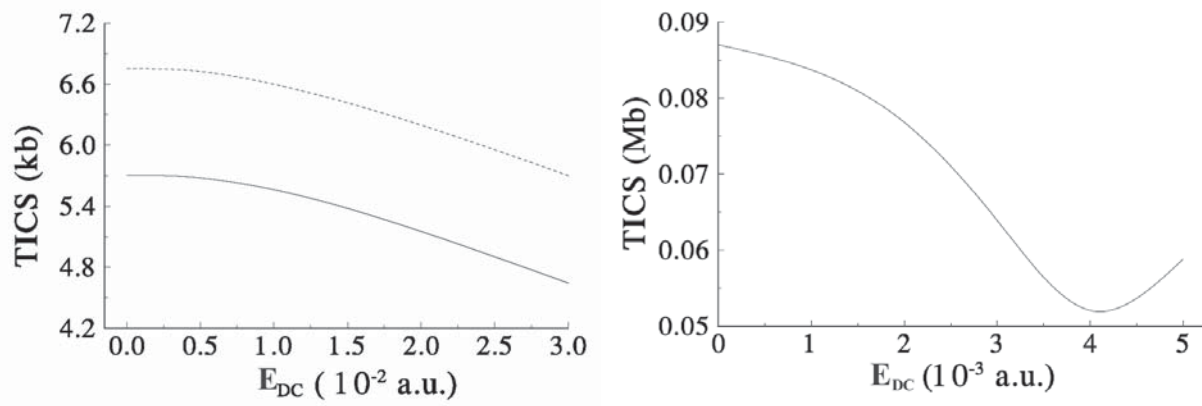


Figure 4.2 Left: TICS of DPI of helium as a function of an external DC field for photon energies of 85 eV (bottom line) and 90 eV (top line). Right: same for H^- at the photon energy of 15 eV.

$J = 0 - 2$ in expansion (4.4). To represent each total angular momentum block, we proceed as in the case of the TPDI calculation described in the previous Section 4.3.

On the left panel of Fig. 4.2 we display the TICS results for DPI at photon energies of 85 eV (bottom curve) and 90 eV (top curve) and various applied DC field strengths. For both frequencies, the TICS exhibits a decrease with the DC field. Such a behaviour is not uncommon for two-electron systems in the external DC electric field when there are alternative routes of decay. We documented a similar behaviour of the total (single plus double) photoionization cross section as a function of the external DC field for helium [22].

A much weaker bound system, H^- , displays a qualitatively different DC field dependence of TICS [23]. This dependence is displayed on the right panel of Fig. 4.2 for the photon energy of 15 eV. As is seen from this figure, the application of even a relatively weak DC field to H^- can produce a considerable change in TICS. As a function of the DC field strength, the TICS reaches a minimum at approximately $E_{DC} = 4 \times 10^{-3}$ a.u. and then starts to grow. The growth of TICS indicates that tunneling ionization due to the DC field is becoming a dominant process. The role of electron correlations at this stage is not very significant. Indeed, an ionization probability behaviour similar to Fig. 4.2 can be obtained already in a simple Keldysh-type model of ionization in the presence of both DC and AC fields [23].

4.5 Strong-field ionization of lithium and hydrogen

Various regimes of strong-field ionization can be conveniently categorized by the adiabaticity Keldysh parameter, which relates the frequencies of atomic motion and the laser field, $\gamma = \omega/\omega_{\text{tunnel}}$ [24]. Alternatively, the Keldysh parameter can be expressed in terms of the atomic ionization potential IP and the ponderomotive

potential U_p , $\gamma = \sqrt{IP/2U_p}$. The MPI regime is characterized by $\gamma \gg 1$, where the characteristic tunneling time of the atomic electron over the Coulomb barrier $\omega_{\text{tunnel}}^{-1}$ is much larger than the timescale ω^{-1} on which electromagnetic field varies considerably. Such a fast ionization process should be described using the quantum-mechanical language of simultaneous absorption of several laser photons. The opposite limit of $\gamma \ll 1$ is reached when the laser field is changing slowly as compared to the characteristic tunneling time. Such a slow adiabatic process can be described quasi-classically using the language of field strength and electron trajectories driven by this field [25].

With increasing field strength and intensity, the width and height of the atomic Coulomb barrier is reduced until it is completely suppressed by the external field. Such a barrier suppression takes place independently of the value of the Keldysh parameter. The lithium atom driven by a femtosecond laser in the near infrared (NIR) spectral range exhibits an unusual example of barrier suppression in the entirely quantum MPI regime. Such a process cannot be treated quasi-classically and analyzed in convenient terms of competing electron trajectories. Instead, a full quantum-mechanical treatment should be given. Because of the large field intensity, such a treatment should be non-perturbative and explicitly time-dependent. Given a large number of field oscillations in the laser pulse and the complexity of the target, an accurate theoretical description of the MPI of Li becomes a challenging task.

In our work [26], we met this challenge by seeking a grid-based solution of the one-electron TDSE by the ALM method, with the local Hamiltonian furnished by an optimized effective potential [27]. We used the velocity gauge to describe the atom-field interaction. The system was enclosed in a box of size $R_{\text{max}} = 2000$ a.u. On the outer boundary of the box the transparent boundary condition was imposed ensuring that edge effects do not appear. The wave function was represented as a series in spherical harmonics (4.3). We included terms with angular momenta up to $\ell_{\text{max}} = 20$ in this expansion. The electron distribution functions were computed by projecting the solution of the TDSE after the end of the pulse on the ingoing distorted waves calculated in the same effective potential.

Results of our calculation are presented in Fig. 4.3 in the form of the photoelectron angular distribution in the polarization plane of laser light. In the momentum distributions shown in this figure, the nominal position of the four-photon line is marked by a dashed semicircle. Four is the minimal number of laser photons $\omega = 1.58$ eV to bridge the ionization potential of the lithium atom $IP = 5.39$ eV. At larger intensities, an additional ring-like structure can be identified due to the five-photon absorption, which is a clear sign of the ATI process. In this process, the photoelectron continues to absorb laser photons when it is already in the ionization continuum. Overall, we see a good agreement between the calculated and experimental spectra in the field intensity range of nearly an order of

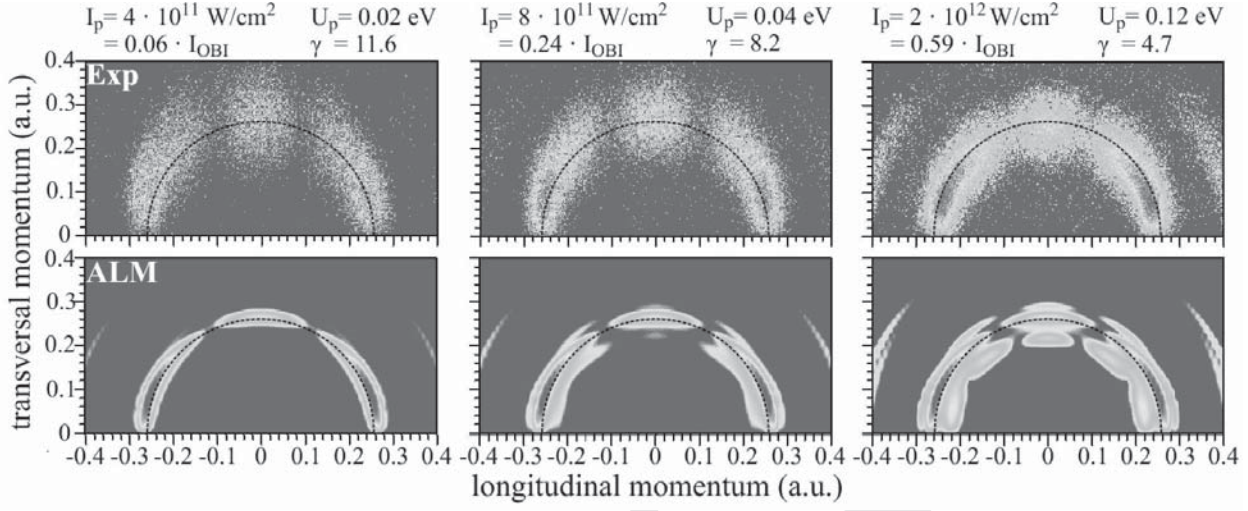


Figure 4.3 Electron momentum distribution parallel (longitudinal) and transversal (perpendicular) to the laser polarization direction. Top row: experimental data obtained by recoil-ion momentum detection. Bottom row: calculated spectra using the ALM model. The laser pulse peak intensity I_p , the ponderomotive potential U_p , and the Keldysh parameter γ are given above each column. The colour scale of the momentum spectra is logarithmic. Dashed semicircle visualizes the nominal position of the four-photon line.

magnitude. Another example of a high non-linearity ionization process is presented by the hydrogen atom driven by an intense NIR laser light [28]. With the intensities reaching 5×10^{14} W/cm², the ATI process takes place with as many as 50 photons being readily absorbed from the laser field. Theoretical description of such a process necessitates a complex numerical simulation in order to achieve a quantitative agreement with the experiment, which was documented at the 10% level in the present case.

In our approach to this problem, as in the case of strong-field ionization of lithium, we employed the Arnoldi–Lanczos propagator scheme. The radial orbitals were defined in a box of size $R_{\max} = 2000$ a.u. With the velocity gauge interaction, the terms with $l < \ell_{\max} = 25$ had to be kept in the expansion (4.3) to ensure convergence.

Our results are presented in Fig. 4.4. The left panel displays an example of a calculated ATI spectrum corresponding to the laser peak intensity of 4×10^{14} W/cm². Each oscillation on this curve corresponds to a single photon absorption. The theoretical data, averaged over the transverse Gaussian profile of the laser beam, are displayed on the right panel for a range of field intensities in comparison with the experimental data [28]. The full set of experimental data points is simultaneously fitted using only two adjustable parameters: an overall scaling factor and an intensity scaling factor. The former factor accounts for the absolute detector efficiency and the target density, which were not independently measured.

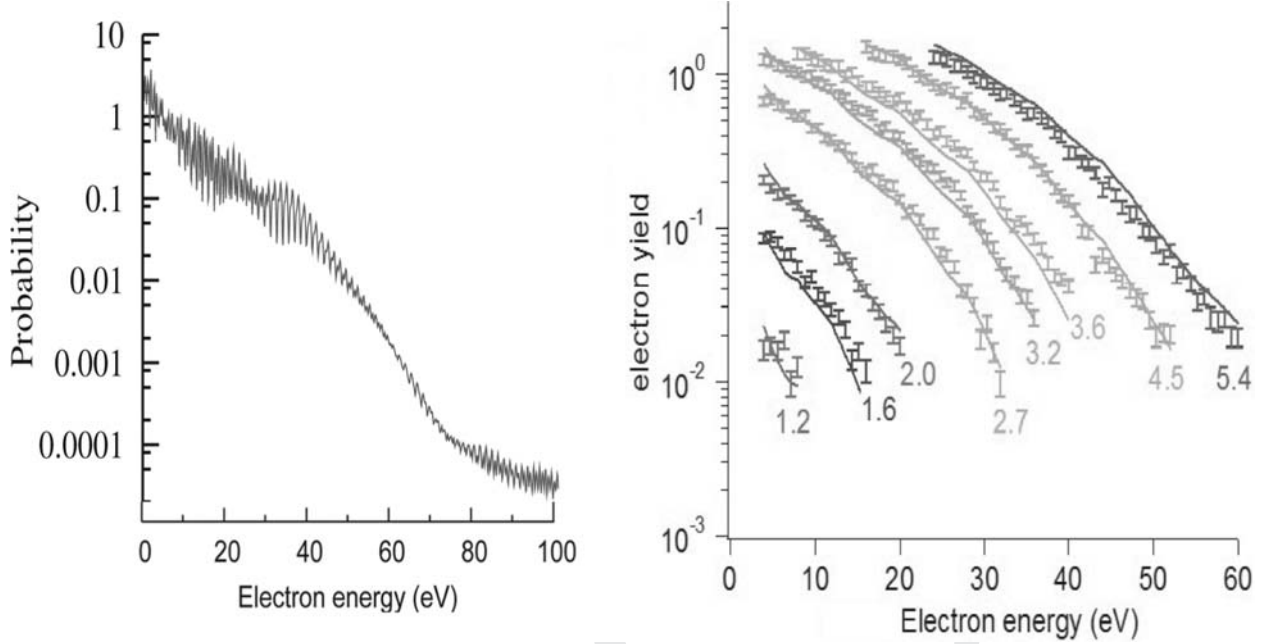


Figure 4.4 The ATI spectrum of atomic hydrogen driven by a 750 nm femtosecond laser. Left: a raw calculated spectrum for laser peak intensity of $4 \times 10^{14} \text{ W/cm}^2$. Right: post-processed theoretical spectra for various peak intensities (solid lines) plotted versus corresponding experimental data (error bars). The laser intensity ranges from 1.2 to $5.4 \times 10^{14} \text{ W/cm}^2$.

The latter factor gives a fit value for the absolute peak intensity, while leaving the relative intensities of the various data runs at their independently measured values. As shown in Fig. 4.2, we obtain agreement at the 10% level between the experimental data and the theoretical prediction over a wide range of electron energies and laser intensities.

4.6 High harmonics generation

High harmonics generation (HHG) is a non-linear atomic process that manifests itself in the appearance of odd-order multiple frequencies in the spectra of an atom placed in an intense electromagnetic field. Many essential features of the HHG process can be explained using the so-called three-step or recollision model [29]. The three steps of this model refer to (i) tunneling ionization of an atomic electron at the moment when the laser field reaches its peak intensity, (ii) acceleration of the photoelectron by the laser field and its return to the parent ion and (iii) recombination with the nucleus and emission of a single HHG photon. The resulting HHG has a typical pattern: the first few quickly decreasing harmonics followed by a plateau ending with a relatively sharp cut-off at the maximum harmonic number, $N_{\text{cut-off}} = (IP + 3.17U_p)/\omega \gg 1$. Up until recently, investigations of the HHG process have been limited to selecting a rare gas atom driven by an NIR laser field to ensure the tunneling ionization regime with the Keldysh parameter $\gamma \simeq 1$. However, a similar HHG regime with $N_{\text{cut-off}} \gg 1$ can be realized in alkaline earth

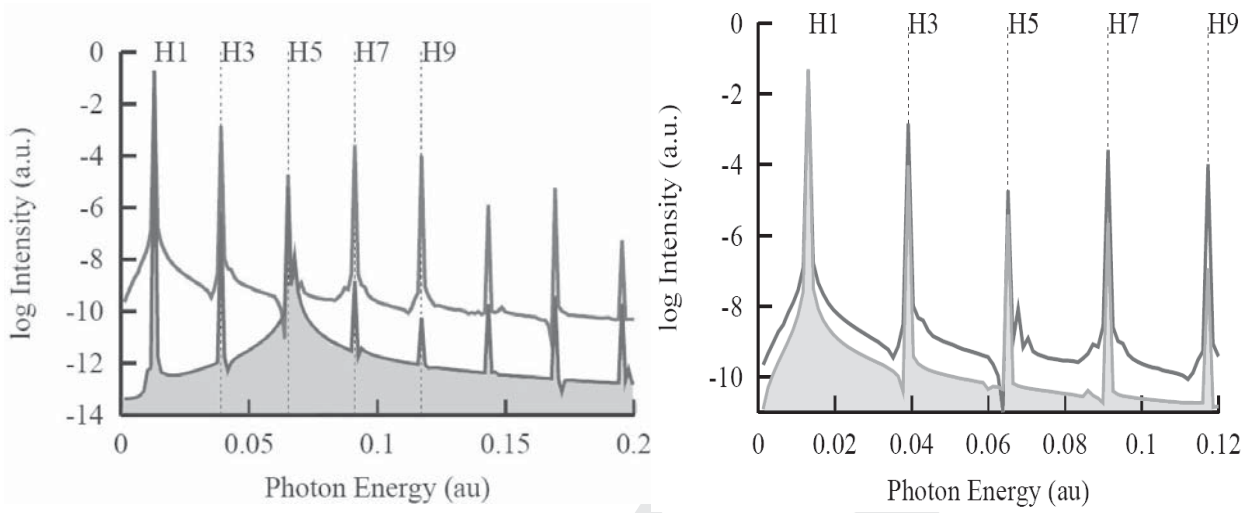


Figure 4.5 Harmonics spectrum of Li driven by a 330 fs laser pulse with the wavelength $\lambda = 3500$ nm. Left panel: the HHG spectrum from the ground $2s$ state at the laser field intensity 8×10^{11} W/cm² (shaded area) and the $2p$ excited state at 2×10^{11} W/cm² (solid line). Right panel: the $2p$ HHG spectrum with the $n\ell$ excited states manifold included (solid line) or excluded (shaded area) from the expansion (4.3).

atoms, which have a much smaller ionization potential, if they are driven by a mid-infrared laser field. In such systems, a strong resonant enhancement of HHG can be observed [30], which is an important factor for possible applications in tabletop sources of highly coherent XUV radiation.

In our approach to the HHG process in alkaline earth atoms (Li [31], Li and K [32], K and Rb [33]), we adopt a single active electron approximation and seek a solution of the TDSE (4.1) with the Hartree–Fock potential of the frozen atomic core on a one-electron basis (4.3). Once the solution of the TDSE is found, the harmonics spectrum is calculated as the Fourier transform of the time-dependent dipole operator [34]:

$$|d(\omega)|^2 = \left| \frac{1}{t_2 - t_1} \int_{t_1}^{t_2} e^{-i\omega t} d(t) dt \right|^2. \quad (4.14)$$

Here, $d(t) = \langle \Psi(t) | z | \Psi(t) \rangle$ is the expectation value of the dipole operator and $\Psi(t)$ is the solution of the TDSE (4.1). In practical computations, the limits of integration t_1, t_2 are chosen to be large enough to minimize the transient effects. In the calculations presented below, we used $t_1 = 20T$, $t_2 = 30T$, i.e., the last 10 cycles of the pulse duration.

An example of resonantly enhanced HHG spectra is presented on the left panel of Fig. 4.5, which correspond to the Li atom prepared in either the ground $2s$ or excited $2p$ state [31]. In the former case, several orders of magnitude in the HHG

intensity can be gained, provided the driving laser field is turned down to avoid the excited state depopulation. To prove the resonant excitation $3p \rightarrow n\ell$ as the main mechanism of the HHG enhancement, we performed several additional computations with the functions $R_{lm}(r, t)$ in expansion (4.3) explicitly orthogonalized to the states of the $n\ell$ manifold. Exclusion of these states causes a sharp drop of the HHG intensity, as is seen on the left panel of Fig. 4.5.

Another way to enhance the HHG spectrum is to extend its cut-off beyond the three-step model limit $N_{\text{cut-off}}$. This can be achieved by tailoring the waveforms of the driving laser pulse. In our recent work [35] we considered an electron moving in a periodic EM field:

$$E(t) = 2\text{Re} \sum_{k=1}^K a_k e^{ik\Omega t}, \quad (4.15)$$

where the requirement of the fixed fluency implies that $4 \sum_{k=1}^K |a_k|^2 = E_0^2$, with the field strength E_0 related to the intensity of the pure cosine wave form via $I = 3.5 \times 10^{16} E_0^2$. Here the field intensity is measured in W/cm^2 and the field strength is expressed in atomic units.

We perform two calculations of this kind. In the first, we impose an additional restriction that only the terms with odd k -values are to be present in Eq. (4.15). This ensures that the resulting HHG spectrum contains only odd harmonics of the main frequency. In the second calculation, we retain the terms with both odd and even k -values in the expansion (4.15). The first calculation was performed with $K = 7$, while in the second we chose $K = 5$.

Results of these calculations, along with the HHG spectrum from a purely cosine waveform, are shown in Fig. 4.6. As one can see from the figure, the set of the parameters corresponding to only odd harmonics allows to achieve a 10% gain in the position of the cut-off. This rather moderate increase is due to essentially the same structure of the classical returning electron trajectories as in the case of the cosine wave. The situation is different for the case of even and odd harmonics present in Eq. (4.15). Here a noticeable extension of the cut-off can be clearly seen.

4.7 Time delay in atomic photoionization

Among other spectacular applications of the attosecond streaking technique, it has become possible to determine the time delay between subjecting an atom to a short XUV pulse and subsequent emission of the photoelectron [36, 37]. With these observations, the question as to when does atomic photoionization actually begin can be answered by the experiment. We have studied this problem theoretically by solving the time-dependent Schrödinger equation and carefully examining the time

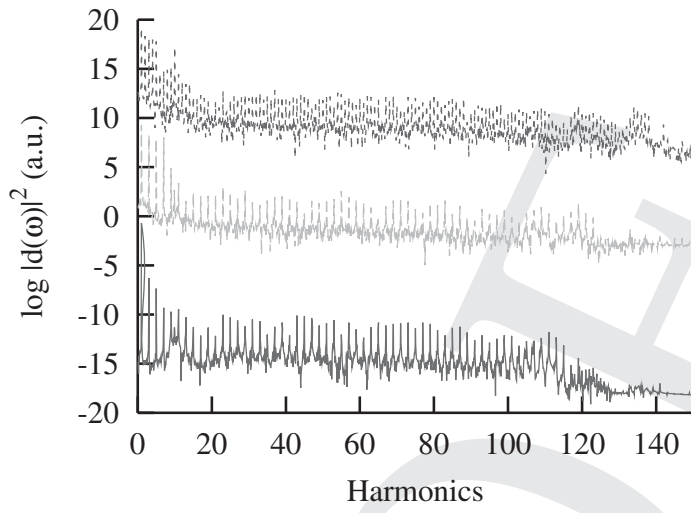


Figure 4.6 Harmonics spectra of Li driven by the laser pulses of different waveforms: the pure cosine wave (bottom); odd harmonics in Eq. (4.15) with $K = 7$ (middle) dashed line, for convenience of comparison the quantity $\log |d(\omega)|^2 + 10$ is shown; odd and even harmonics in Eq. (4.15) with $K = 5$ (top), the quantity $\log |d(\omega)|^2 + 20$ is shown.

evolution of the photoelectron wave packet. In this way we established the apparent ‘time zero’ when the photoelectron left the atom. At the same time, we provided a stationary treatment to the photoionization process and connected the observed time delay with the quantum phase of the dipole transition matrix element, the energy dependence of which defines the emission timing. We applied this timing analysis to valence shell single photoionization of neon [38] and DPI of helium [39].

In the case of Ne, we solve a one-electron TDSE (4.1) with the field-free atomic Hamiltonian \hat{H}_{atom} defined by the parameterized optimized effective potential [27]. The TDSE is solved by radial grid integration using the MIM method. The solution of the TDSE is used to form the wave packet representing the photoelectron ejected from a given shell:

$$\Phi(\mathbf{r}, t) = \sum_L \int a_{kL}(t) \chi_{kL}(\mathbf{r}) e^{-iE_k t} dk. \quad (4.16)$$

Here, $a_{kL}(t) = e^{iE_k t} \langle \chi_{kL} | \Psi(t) \rangle$ are the projection coefficients of the solution of the TDSE on the continuum spectrum of the atom. This solution corresponds to the initial condition $\Psi(t = 0) \rightarrow \Psi_i$, where i indicates the atomic shell to be ionized. The continuum state $\chi_{kL}(\mathbf{r}) = R_{kl}(r) Y_L(\mathbf{r}/r)$ is the product of the radial orbital with the asymptotic

$$R_{kl} \propto \sin [kr + \delta_l(k) + 1/k \ln(2kr) - l\pi/2]$$

and the spherical harmonic $Y_L(\mathbf{r}/r)$ with $L \equiv l, m$.

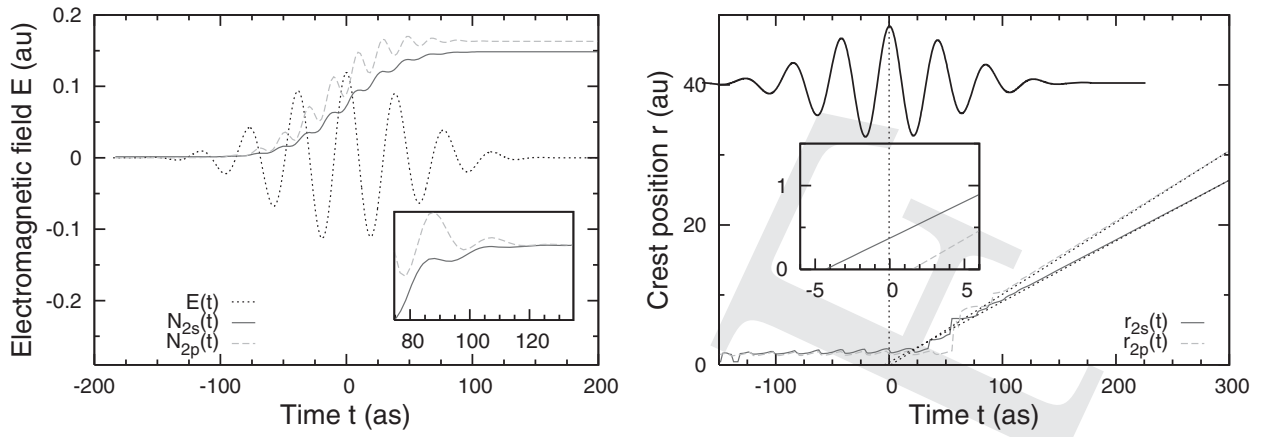


Figure 4.7 Left panel: the norm of the wave packets $N(t)$ (scaled arbitrarily) emitted from the $2s$ and $2p$ sub-shells of Ne is plotted as a function of time with the solid and dashed lines, respectively. The XUV pulse is over-plotted with the black dotted line. In the inset, the norm variation $[N(t) - N(T_1)]/N(T_1)$ is shown on an expanded timescale near the pulse end. Right panel: the crest position of the $2s$ and $2p$ wave packets is shown with the same line styles. The crest position after the pulse end is fitted with the straight line, which corresponds to the free propagation. In the inset, extrapolation of the free propagation inside the atom is shown.

We use two convenient indicators of the evolution of the wave packet. One is the norm given by the integral $N(t) = \sum_L \int dk |a_{kL}(t)|^2$. This norm is plotted on the left panel of Fig. 4.7, with the solid and dashed lines for the wave packets originating from the $2s$ and $2p$ sub-shells, respectively. For better clarity, these curves are scaled and over-plotted on the electromagnetic pulse. The figure shows clearly that the evolution of the $2s$ and $2p$ wave packets starts and ends at the same time without any noticeable delay. This is further visualized in the inset where the variation of the norm $[N(t) - N(T_1)]/N(T_1)$ is plotted on an expanded timescale near the driving pulse end. Indeed, the norm starts deviating from zero with the rise of the XUV pulse and reaches its asymptotic value once the interaction with the XUV pulse is over.

Another marker of the wave-packet dynamics is the crest position, defined as a location of the global maximum of the electron density. The latter quantity is truly informative only when the electron is outside the atom and the wave packet is fully formed, having one well-defined global maximum. On the right panel of Fig. 4.7, we show the crest position of the $2s$ and $2p$ wave packets propagating in time. We see that evolution of the norm and the movement of the crest commence at about the same time. The movement of the crest becomes almost linear when the norm reaches its asymptotic value and the wave packet is fully formed. Once fitted with the linear time-dependence $r = k(t - t_0) + r_0$ for large times $t > T_1$ (shown as a dotted straight line) and back propagated inside the atom, the $2s$ wave packet seems to have an earlier start time t_0 than that of the $2p$ wave packet. This difference is magnified in the inset.

We see that at the origin $t_0^{2s} < 0$ and $t_0^{2p} > 0$ are shifted to the opposite direction with respect to the peak of the driving XUV pulse, which sets the start time of the photoionization process. We relate the opposite signs of the time delays with the energy dependence of the corresponding scattering phases $\delta_{l=1}^{2s}$ and $\delta_{l=2}^{2p}$, which is governed by the Levinson–Seaton theorem [40].

In the case of DPI of He, we solve a two-electron TDSE using the ALM method. The field-free solution of the TDSE at $t > T_1$ is used to construct a two-electron wave packet $\Psi_1(\mathbf{r}_1, \mathbf{r}_2, t)$ with the asymptotics corresponding to the given photoelectron momenta $\mathbf{k}_1, \mathbf{k}_2$:

$$\Psi_1(\mathbf{r}_1, \mathbf{r}_2, t) = \hat{P}_{\mathbf{k}_1, \mathbf{k}_2} \Psi(\mathbf{r}_1, \mathbf{r}_2, t). \quad (4.17)$$

Here, the kernel of the projection operator is constructed as

$$\langle \mathbf{r}'_1, \mathbf{r}'_2 | \hat{P}_{\mathbf{k}_1, \mathbf{k}_2} | \mathbf{r}_1, \mathbf{r}_2 \rangle = \int_{\Omega} \Psi_{q_1}^-(\mathbf{r}_1) \Psi_{q_2}^-(\mathbf{r}_2) \Psi_{q_1}^-(\mathbf{r}'_1)^* \Psi_{q_2}^-(\mathbf{r}'_2)^* d\mathbf{q}_1 d\mathbf{q}_2, \quad (4.18)$$

where $\Psi_{k_i}^-(\mathbf{r}_i), i = 1, 2$ are one-electron scattering states with the ingoing boundary condition describing a photoelectron moving in the Coulomb field with $Z = 2$.

The wave packet function $\Psi_1(\mathbf{r}_1, \mathbf{r}_2, t)$ is plugged into the one-electron density function

$$\rho(\mathbf{r}, t) = \int |\Psi_1(\mathbf{r}_1, \mathbf{r}_2, t)|^2 [\delta(\mathbf{r} - \mathbf{r}_1) + \delta(\mathbf{r} - \mathbf{r}_2)] d\mathbf{r}_1 d\mathbf{r}_2. \quad (4.19)$$

The maxima of this density function are then traced to determine the trajectories of both photoelectrons which, at large distances, can be approximated by

$$r_i(t) - k_i t - r'_i(t) \asymp k_i t_{0i}. \quad (4.20)$$

Here t_{0i} are the time delays and $r'_i(t)$ are known functions which vary logarithmically slow with t .

An example of our timing analysis is illustrated in Fig. 4.8. Here we consider a DPI process in which one photoelectron escapes with energy 32 eV along the z -axis and another with energy 10 eV along the x -axis, thus sharing the excess energy of 42 eV, which corresponds to the photon energy $\omega = 121$ eV. A sequence of snapshots of the one-electron density function (4.19) is taken with an interval of $2T$ and the maxima of the electron density are traced in time. With the known logarithmic function $r'_i(t)$, this procedure defines the trajectories $r_i(t) - r'_i(t)$ for both photoelectrons, which are exhibited on the left panel of Fig. 4.8. The raw data, shown by the points, are fitted with the straight lines $k_z(t - t_0)$ and $k_x(t - t_0)$, which visualize the free propagation. The intersect of these straight lines with the abscissa gives the corresponding time delays t_{0i} . We ran an analogous simulation for other

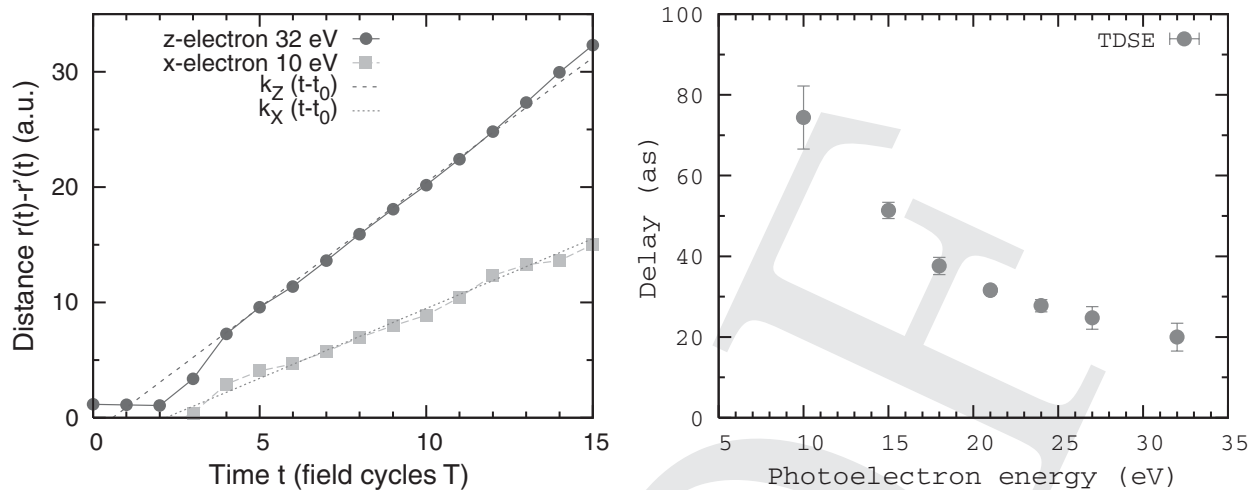


Figure 4.8 Left panel: trajectories of 32 eV and 10 eV photoelectrons propagating along the z and x axes, respectively. The co-ordinates of both photoelectrons, measured with intervals of two field cycles, are shown as dots. The straight lines visualize the free propagating $k_z(t - t_0)$ and $k_x(t - t_0)$. Right panel: time delay as a function of the photoelectron energy.

energy-sharing cases. Thus obtained time-delay data are collated on the right panel of Fig. 4.8. The error bars indicate the uncertainty of the fitting procedure.

The rapid change of the time delay with increase of the photoelectron energy corresponds to the crossover between the two leading mechanisms of DPI: the fast shake-off (SO) and the slow knock-out (KO) processes. The SO mechanism is driven by a fast rearrangement of the atomic core after departure of the primary photoelectron. The KO mechanism involves repeated interaction of the primary photoelectron with the remaining electron bound to the singly charged ion. Thus, future attosecond-delay measurements on DPI of He can provide information on the absolute quantum phase and elucidate various mechanisms of this strongly correlated ionization process.

References

- [1] A. Becker, R. Dörner and R. Moshhammer, *J. Phys. B*, **38**, S753 (2005).
- [2] D. A. Varshalovich, A. N. Moskalev, and V. K. Khersonskii, *Quantum Theory of Angular Momentum* (Singapore: World Scientific, 1988).
- [3] E. Cormier and P. Lambropoulos, *J. Phys. B*, **29**, 1667 (1996).
- [4] W. Magnus, *Comm. Pure and Appl. Math.*, **7**, 649 (1954).
- [5] T. J. Park and J. C. Light, *J. Chem. Phys.*, **85**, 5870 (1986).
- [6] D. Dundas, *Phys. Rev. A*, **65**, 023408 (2002).
- [7] M. Nurhuda and F. H. M. Faisal, *Phys. Rev. A*, **60**, 3125 (1999).
- [8] H. Hasegawa, E. J. Takahashi, Y. Nabekawa, K. L. Ishikawa and K. Midorikawa, *Phys. Rev. A*, **71**, 023407 (2005).
- [9] Y. Nabekawa, H. Hasegawa, E. J. Takahashi and K. Midorikawa, *Phys. Rev. Lett.*, **94**, 043001 (2005).

- [10] A. A. Sorokin, M. Wellhofer, S. V. Bobashev, K. Tiedtke, and M. Richter, *Phys. Rev. A*, **75**, 051402 (2007).
- [11] P. Antoine *et al.*, *Phys. Rev. A*, **78**, 023415 (2008).
- [12] I. A. Ivanov and A. S. Kheifets, *Phys. Rev. A*, **75**, 033411 (2007).
- [13] I. Bray, *Phys. Rev. A*, **49**, 1066 (1994).
- [14] I. A. Ivanov and A. S. Kheifets, *Phys. Rev. A*, **74**, 042710 (2006).
- [15] I. Bray and A. T. Stelbovics, *Adv. Atom. Mol. Phys.*, **35**, 209 (1995).
- [16] D. A. Horner, F. Morales, T. N. Rescigno, F. Martin, and C. W. McCurdy, *Phys. Rev. A*, **76**, 030701(R) (2007).
- [17] J. Feist *et al.*, *Phys. Rev. A*, **77**, 043420 (2008).
- [18] X. Guan, K. Bartschat and B. I. Schneider, *Phys. Rev. A*, **77**, 043421 (2008).
- [19] I. A. Ivanov, A. S. Kheifets and J. Dubau, *Eur. Phys. J. D*, **61**, 563 (2011).
- [20] J. S. Briggs and V. Schmidt, *J. Phys. B*, **33**, R1 (2000).
- [21] L. Avaldi and A. Huetz, *J. Phys. B*, **38**, S861 (2005).
- [22] I. A. Ivanov and A. S. Kheifets, *Eur. Phys. J. D*, **38**, 471 (2006).
- [23] I. A. Ivanov and A. S. Kheifets, *Phys. Rev. A*, **75**, 062701 (2007).
- [24] L. V. Keldysh, *Sov. Phys. -JETP*, **20**, 1307 (1965).
- [25] P. B. Corkum, *Phys. Rev. Lett.*, **71**, 1994 (1993).
- [26] M. Schuricke *et al.*, *Phys. Rev. A*, **83**, 023413 (2011).
- [27] A. Sarsa, F. J. Gálvez and E. Buendia, *Atomic Data and Nuclear Data Tables*, **88**, 163 (2004).
- [28] M. G. Pullen *et al.*, *Opt. Lett.*, **36**, 3660 (2011).
- [29] P. B. Corkum, *Phys. Rev. Lett.*, **71**, 1994 (1993).
- [30] P. M. Paul *et al.*, *Phys. Rev. Lett.*, **94**, 113906 (2005).
- [31] I. A. Ivanov and A. S. Kheifets, *J. Phys. B*, **41**, 115603 (2008).
- [32] I. A. Ivanov and A. S. Kheifets, *J. Phys. B*, **42**, 145601 (2009).
- [33] I. A. Ivanov and A. S. Kheifets, *Phys. Rev. A*, **79**, 053827 (2009).
- [34] J. L. Krause, K. J. Schafer and K. C. Kulander, *Phys. Rev. A*, **45**, 4998 (1992).
- [35] I. A. Ivanov and A. S. Kheifets, *Phys. Rev. A*, **80**, 023809 (2009).
- [36] M. Schultze *et al.*, *Science*, **328**, 1658 (2010).
- [37] K. Klünder *et al.*, *Phys. Rev. Lett.*, **106**, 143002 (2011).
- [38] A. S. Kheifets and I. A. Ivanov, *Phys. Rev. Lett.*, **105**, 233002 (2010).
- [39] A. S. Kheifets, I. A. Ivanov and I. Bray, *J. Phys. B*, **44**, 101003 (2011).
- [40] L. Rosenberg, *Phys. Rev. A*, **52**, 3824 (1995).